A High-Resolution Air Pollution Model Suitable for Dispersion Studies in Complex Terrain

MING LIU AND JOHN J. CARROLL

Department of Land, Air and Water Resources, University of California, Davis, Davis, California

(Manuscript received 4 October 1995, in final form 25 March 1996)

ABSTRACT

The development of an air pollution transport model that uses an expanding terrain-following coordinate with high resolution in analytic form near the surface and a high-order accurate transport algorithm is described. The model is designed to be internally consistent in the application of numerical methods, computationally efficient, and suitable for pollutant dispersion studies in complex terrain. The application of the time-splitting Warming–Kutler–Lomax advection scheme is examined in both rotational and deformational flows for its conservation and stability properties. It is found that the combination of this scheme with a short-wave filter makes the integration mass conserving and dispersion free. The model is applied to some hypothetical cases that represent the typical phenomena occurring over mountains. The model proves to be capable of simulating realistic planetary boundary layer structure and stability variation, hydrostatic mountain waves, thermally induced mountain–valley winds, and passive scalar dispersion over sloped surfaces reproducing features observed in field experiments.

1. Introduction

There are a number of numerical models available for use by the meteorological community, for example, the NCAR Community Climate Model, CSU–RAMS, Penn State–NCAR MM5, UO/NSSC-ARPS, and others. Each of these was constructed and optimized to simulate specific kinds of meteorological phenomena, but none specifically for simulation of air pollutant dispersion in complex terrain. The primary requirements for such a model are that 1) mass of pollutants be conserved; 2) the surface-layer fluxes and stability variations be reasonably well calculated; 3) the planetary boundary layer (PBL) structure be well resolved; and 4) slope flows, especially drainage flows, be accurately described. These requirements in turn require that the model have high resolution near the surface and moderate resolution aloft; and that the pressure gradients computed over the sloping surfaces be very accurate. This paper describes the design of such an air pollution transport model; the tests performed to evaluate its properties relative to these requirements, and its application to an idealized pollutant dispersion problem. We assume the hydrostatic approximation is valid for this kind of meteorological system in which horizontal motions greatly exceed vertical motions (Pielke 1984), such as circulations over relatively gentle slopes, and for horizontal resolutions as small as 10 km (Wippermann 1981).

Variation of the radiation budget coupled with turbulent exchange are primarily responsible for the PBL diurnal evolution. High-order turbulence closure models and large-eddy simulation models by Andre et al. (1978), Moeng (1984), and many others, describe turbulence effects in detail and provide good understanding of the PBL dynamics. However, they are computationally expensive. For operational purposes, simplified, lower-order closure models are attractive. One simple method is to prescribe an eddy diffusivity K as a profile based on bulk layer stability, such as O'Brien's cubic polynomial (1970). Another is the use of local Richardson (Ri) number, such as Blackadar's scheme (1979), in which K is defined by the local wind and temperature gradients. We believe locally Ri-dependent diffusivities are more desirable representations of subgrid-scale turbulent mixing. Carroll (1993) has shown that if high resolution is used near the surface, the strong curvature of mean profiles there can be reproduced and simple first-order closure yields realistic PBL behavior. Pragmatically, this requires the use of an expanding grid mesh near the surface. An important question is how to maintain the accuracy of finite difference algorithms in such a grid space. Numerical methods achieve their best accuracy when applied to an equally spaced grid mesh; this is especially true for high-order methods that use information from multiple grid points. In this model, as in Carroll's (1993), the grid space is expanded quickly in a logarithmic coor-

Corresponding author address: John J. Carroll, Department of Land, Air and Water Resources, University of California, Davis, Davis, CA 95616.
E-mail: Carroll@atm1.ucdavis.edu

© 1996 American Meteorological Society

dinate with constant increment. This allows an analytical transformation of coordinates and a full expression of derivatives, which can then be discretized over equal grid sizes defined in the transformed system.

Terrain-following coordinates are used to simplify lower boundary conditions in irregular topography. The transformed coordinates are normally specified as normalized forms of pressure, potential temperature, or height. The disadvantage of pressure and temperature coordinates is that both surface pressure and temperature are functions of time, requiring tendency terms for the transformations. A common problem with terrain-following coordinates is the calculation of horizontal pressure gradients (Mesinger and Janjic 1985). This problem results from inaccurate integration of the hydrostatic equation or inconsistencies in the calculation of horizontal pressure gradients in those coordinates. Carroll et al. (1987) proposed the use of analytic integration of the hydrostatic equation for both the grid-point pressure and the vertical variation of pressure along a tilted surface to obtain more accurate pressure gradient calculations. By using this algorithm, the model described here minimizes internal pressure calculation errors in a height ratio terrain-following coordinate.

The numerical integration of advection terms is critical to the quality of the model solutions. One common way of choosing an advection scheme is to consider its numerical dissipation and dispersion properties, as well as its computational efficiency. The second-order leapfrog and Lax–Wendroff schemes have the shortcoming of strong dispersion if unfiltered, which leads to noisy or unstable solutions. Most higher-order advection schemes, such as the two-step Takacs scheme (1985), and the combined backward and forward McCormick scheme (R.-Mendez-Nuñez and Carroll 1993), use predictor–corrector sequences to reduce numerical errors. Purnell (1976) developed a global method that uses cubic-spline curve fitting for a Lagrangian upstream interpolation and solves a coefficient matrix. Some positive definite advection schemes have been commonly used for scalar quantities, among them is Smolarkiewicz's (1984) iterative flux-corrected procedure of antidiffusion and antidispersion applied to upstream advection. Though these schemes have good amplitude and phase properties, they are complex and expensive computationally. Our recent experience has let us to favor the use of a one-step Warming–Kutler–Lomax (WKL) scheme (Anderson et al. 1984; Huang and Raman 1991, hereafter HR) that is third- to fourth-order accurate. Momentum and temperature fields normally require some numerical diffusion to obtain stable integration; while mixing ratios or concentrations need good mass conservation especially for long-range transport. The WKL scheme can satisfy these different needs by selective control of a free parameter in the scheme. Huang and Raman proposed a modified multidimensional WKL algorithm by including a cross-space correction term, and a positive definite method of deleting negative values and applying heavy damping to nearby positive values for compensation. In this study, HR's proposals are challenged and the WKL scheme is further investigated for its application in an air pollution transport model.

2. Model description

a. Model equations

The model uses a height ratio terrain-following coordinate $z^* = h(z - z_g)(h - z_g)^{-1}$ to treat an irregular lower boundary, where h is the height of model domain and $z_g(x, y)$ the topographic height. The Exner function $[\pi = C_p(P/P_0)^{R_d/C_p}]$ is used for pressure to eliminate density from the governing equations. The horizontal momentum equations in a three-dimensional system are

$$\frac{\partial u}{\partial t} + u\left.\frac{\partial u}{\partial x}\right|_{z^*} + v\left.\frac{\partial u}{\partial y}\right|_{z^*} + w^*\frac{\partial u}{\partial z^*} = fv + \left(\frac{h}{h - z_g}\right)^2 \frac{\partial}{\partial z^*}\left(K_m \frac{\partial u}{\partial z^*}\right)^2 - \theta\left(\left.\frac{\partial \pi}{\partial x}\right|_{z^*} - \frac{h - z^*}{h - z_g}\frac{\partial \pi}{\partial z^*}\frac{\partial z_g}{\partial x}\right) \quad (1)$$

$$\frac{\partial v}{\partial t} + u\left.\frac{\partial v}{\partial x}\right|_{z^*} + v\left.\frac{\partial v}{\partial y}\right|_{z^*} + w^*\frac{\partial v}{\partial z^*} = -fu + \left(\frac{h}{h - z_g}\right)^2 \frac{\partial}{\partial z^*}\left(K_m \frac{\partial v}{\partial z^*}\right)^2 - \theta\left(\left.\frac{\partial \pi}{\partial y}\right|_{z^*} - \frac{h - z^*}{h - z_g}\frac{\partial \pi}{\partial z^*}\frac{\partial z_g}{\partial y}\right); \quad (2)$$

the hydrostatic equation is

$$\frac{\partial \pi}{\partial z^*} = -\frac{h - z_g}{h}\frac{g}{\theta}; \quad (3)$$

the continuity equation is

$$\frac{\partial u(h - z_g)}{\partial x} + \frac{\partial v(h - z_g)}{\partial y} + \frac{\partial w^*(h - z_g)}{\partial z^*} = 0; \quad (4)$$

the thermodynamic energy equation is

$$\frac{\partial \theta}{\partial t} + u\left.\frac{\partial \theta}{\partial x}\right|_{z^*} + v\left.\frac{\partial \theta}{\partial y}\right|_{z^*} + w^*\frac{\partial \theta}{\partial z^*} = \left(\frac{h}{h - z_g}\right)^2 \frac{\partial}{\partial z^*}\left(K_h \frac{\partial \theta}{\partial z^*}\right)^2 - \frac{h}{h - z_g}\frac{\theta}{\rho T C_p}\frac{\partial R_n}{\partial z^*}; \quad (5)$$

and the conservation equation for scalar concentration or mixing ratio c is

$$\frac{\partial c}{\partial t} + u\left.\frac{\partial c}{\partial x}\right|_{z^*} + v\left.\frac{\partial c}{\partial y}\right|_{z^*} + w^*\frac{\partial c}{\partial z^*} = \left(\frac{h}{h - z_g}\right)^2 \frac{\partial}{\partial z^*}\left(K_h \frac{\partial c}{\partial z^*}\right)^2 + S(c), \quad (6)$$

where R_n is the net longwave radiation flux in the vertical, and $S(c)$ the source or sink term. The relationship between w and w^* is given by

$$w^* = \frac{h}{h - z_g} w + \frac{z^* - h}{h - z_g}\left(u\frac{\partial z_g}{\partial x} + v\frac{\partial z_g}{\partial y}\right). \quad (7)$$

In these equations, u, v, w, θ, and c are all resolvable-scale variables. The horizontal subgrid-scale fluxes are assumed negligible. In this model, numerical stability is controlled by a parameter in the advection scheme as discussed below, which can provide numerical diffusion required for stable integration. The longwave radiative transfer in the thermodynamic energy equation (5) is calculated based on the emissions from H_2O, CO_2, and O_3. Sasamori's full implementation method (1968, 1972) is used to parameterize the emission and absorption.

b. Vertically expanding grid mesh

A logarithmic, expanding coordinate $\xi = \ln(z^*/d_0 + 1)$ is further applied to the z^* coordinate, where d_0 is a scaling parameter. This allows the high resolution in the lower part of model domain needed to resolve strong curvature of profiles in the surface layer and to produce appropriate turbulent fluxes there. The integration of vertical turbulent diffusion and advection for any φ field in the ξ coordinate becomes

$$\frac{\partial \phi}{\partial t} = \frac{1}{d_0 + z^*}\frac{\partial}{\partial \xi}\left(\frac{K}{d_0 + z^*}\frac{\partial \phi}{\partial \xi}\right) - \frac{w^*}{d_0 + z^*}\frac{\partial \phi}{\partial \xi}. \quad (8)$$

In Eq. (8), $(d_0 + z^*)^{-1}$ appears as a correction for each derivative in the vertical, so that all the gradients can be discretized in a constant $\Delta\xi$ grid space to conserve energy in the diffusion calculation. The WKL advection scheme is applied in this transformed coordinate with the variables being advected by the corrected velocity, $w^*(d_0 + z)^{-1}$, thus preserving the mass conservation properties of the scheme.

By choosing d_0 and $\Delta\xi$, as well as the number of expanding grid layers, one can define an expanding grid mesh up to a predetermined height with the last grid layer having a specified depth, Δz^*. Above this height, a constant grid space having the same Δz^* is used. This is required to properly match the spatial derivatives between the expanding and fixed grid regions. Because z^* can be expressed in terms of ξ analytically and expanded with constant $\Delta\xi$ in the calculation, this coordinate transformation does not add much complexity to the numerical code and maintains the accuracy of numerical schemes used in the model. In the following numerical experiments, the resolution is set such that $\Delta z^* = 14.8, 16.4, 18.0, 19.9, 21.9, 24.1\cdots$. The expanding part has 31 grid layers and extends to a height of 2800 m, above which a constant $\Delta z^* = 300$ is used.

c. Turbulence parameterization and surface energy budget

Eddy diffusivities K_m and K_h in Eqs. (1), (2), (5), and (6) are calculated using Blackadar's local Ri number dependent scheme (1979), where for stable conditions

$$K_m = K_h = l^2 s\left(1 - \frac{\mathrm{Ri}}{\mathrm{Ri}_c}\right)^2 \quad (9)$$

and for unstable conditions

$$K_m = l^2 s(1 - 21\ \mathrm{Ri})^{1/2}, \quad K_h = l^2 s(1 - 87\ \mathrm{Ri})^{1/2}, \quad (10)$$

$\mathrm{Ri} = g(\partial\theta/\partial z)(\theta s^2)^{-1}$, $\mathrm{Ri}_c = 0.25$ is the critical Richardson number, and s the local vector wind shear. The mixing length l is computed from the formula $l = 0.4z(1 + 0.4z/\lambda)^{-1}$ with $\lambda = 80$ m in the numerical experiments described below. The parameterization of vertical subgrid-scale fluxes in the free atmosphere uses the same scheme as in the PBL, but the mixing length is chosen larger than that of the PBL, such as 50%–70% of the grid-layer size.

The change of temperature at the surface is found by evaluating a surface energy budget coupled with a soil layer, in which the net incoming global solar radiation is computed by a bulk transmissivity model (Carroll 1985), and the downward longwave radiation is obtained from the same computation as for the radiative fluxes in the thermodynamic equation (5). The surface turbulent momentum, sensible heat, and moisture fluxes are solved by Monin–Obukhov similarity theory with the nondimensional flux-profile relationships of Businger et al. (1971). We use the analytical solutions provided by Byun (1990) for the similarity equations to obtain turbulent fluxes in the surface layer.

A soil layer, 1 m thick, is included in the model to serve as a heat reservoir, the bottom of which remains at a constant temperature. The same form of vertical logarithmic coordinate as used in the air is also employed in the soil to obtain 11 expanding grid layers from the top ($\Delta z_s = 0.0093$ m) to the bottom ($\Delta z_s = 0.30$ m). The soil temperature T_s is computed from the Fourier equation expressed in the expanding coordinate as

$$\frac{\partial T_s}{\partial t} = \frac{K_s}{(d_0 + z_s)^2}\left(\frac{\partial^2 T_s}{\partial \xi^2} - \frac{\partial T_s}{\partial \xi}\right), \quad (11)$$

where K_s is soil heat diffusivity and z_s the depth in the soil layer. The ground heat flux in the surface energy

budget is then calculated based on the soil temperature gradient. Equation (11) and all turbulent diffusion terms in (1), (2), (5), and (6) are integrated in time using the Crank–Nicolson semi-implicit method.

The turbulence parameterization scheme (Blackadar 1979) coupled with the surface energy budget was tested against the diurnal evolution of the Wangara PBL on experimental day 33–34 (Clarke et al. 1971) by Liu (1994). The calculated mean variable profiles were in very good agreement with the observations, and the subgrid-scale flux profiles and surface stability variables were comparable with those obtained by higher-order turbulence closure models. This reaffirms the results of Carroll (1993) that with high resolution near the surface, a local Ri number–dependent scheme effectively simulates realistic PBL structure and variation.

d. *Pressure calculation and boundary conditions*

The horizontal pressure gradient in the terrain-following coordinate is calculated using an accurate methodology proposed by Carroll et al. (1987), in which the vertical potential temperature profile is defined to be piecewise linear within each grid layer, allowing analytical integration of the hydrostatic equation; that is,

$$\pi_k = \begin{cases} \pi_{k+1} + \dfrac{h - z_g}{h}\dfrac{g}{\gamma_k}\ln\dfrac{\theta_{k+1}}{\theta_k}, & \gamma_k \neq 0 \\ \pi_{k+1} + \dfrac{h - z_g}{h}\dfrac{g}{\theta_k}(z^*_{k+1} - z^*_k), & \gamma_k = 0, \end{cases} \tag{12}$$

where γ_k is the potential temperature gradient in the $z^*(x, y)$ coordinate. Using this methodology, the model was tested under the initial condition of zero velocity, and horizontally uniform temperature distribution with a vertical temperature gradient 4 K km^{-1} over a bell-shaped mountain 1 km high and 400 km wide. The maximum horizontal wind speed resulting from errors in the pressure gradient calculation is found to be 10^{-10} m s^{-1} after a 4-h integration.

The model's physical domain is about 8.5 km deep and is expandable if necessary. Above that a layer is added to absorb upward propagating gravity wave energy before it reaches a rigid upper boundary. The absorbing terms use a sinusoidal profile of viscosity:

$$\nu = \nu_T \sin^2\left(\frac{\pi}{2}\frac{z^* - z^*_B}{z^*_T - z^*_B}\right), \tag{13}$$

where $\nu_T = 1$, and z^*_B and z^*_T are the height at the bottom and top of the absorbing layer. According to Klemp and Lilly (1978), the sinusoidal profile of viscosity produces smaller reflections at the upper boundary than linear profiles such as $\nu = \nu_T(z^* - z^*_B)(z^*_T - z^*_B)^{-1}$.

At the lateral boundaries, a radiation boundary condition (Miller and Thorpe 1981) combined with a minimum phase speed of Hedley and Yau (1988) is used to obtain the maximum outward propagation of disturbances. The phase speed C^* is defined in such a way that a broad range of disturbances in a φ field are advected at C^* out of a lateral boundary with the minimum reflection; that is,

$$C^* = \max\left(\frac{\Delta x}{\Delta t}\frac{\phi^{n+1}_{B-1} - \phi^n_{B-1}}{\phi^n_{B-2} - \phi^n_{B-1}}, C^*_{\min}\right), \tag{14}$$

where φ_B, φ_{B-1}, and φ_{B-2} are the boundary point and the inner points next to the boundary, respectively, and $C^* \leqslant \Delta x/\Delta t$ for numerical stability. Here, $C^*_{\min}$ is a minimum phase speed used to prevent the situation where information cannot propagate outward due to very small or zero local gradients at the boundary and help to reduce the variation of phase speed in the vertical. Here, $C^*_{\min}$ is taken as half of the maximum phase speed of propagating gravity waves and is about 5–10 m s^{-1} in our numerical experiments.

3. Advection scheme

The advection terms in the model are solved by a Crowly type of Warming–Kulter–Lomax (WKL) scheme (Anderson et al. 1984; HR 1991). This is a one step, two time level algorithm having the discrete form in one dimension given by

$$\begin{aligned}\phi^{n+1}_i = \phi^n_i &- \frac{\alpha}{12}(-\phi^n_{i+2} + 8\phi^n_{i+1} - 8\phi^n_{i-1} + \phi^n_{i-2}) \\ &+ \frac{\alpha^2}{8}(\phi^n_{i+2} - 2\phi^n_i + \phi^n_{i-2}) \\ &+ \frac{\alpha^3}{12}(-\phi^n_{i+2} + 2\phi^n_{i+1} - 2\phi^n_{i-1} + \phi^n_{i-2}) \\ &- \frac{\omega}{24}(\phi^n_{i+2} - 4\phi^n_{i+1} + 6\phi^n_i - 4\phi^n_{i-1} + \phi^n_{i-2}),\end{aligned} \tag{15}$$

where ω is a free parameter, and α the local Courant number $(u\Delta t/\Delta x)$. The conditions of $|\alpha_{\max}| \leqslant 1$ and $4\alpha^2 - \alpha^4 \leqslant \omega \leqslant 3$ are required for stable solutions. The truncation error analysis given in HR shows that when $\omega = \omega_1 = 4\alpha^2 - \alpha^4$, the scheme is fourth-order accurate with minimum dissipation; whereas when $\omega = \omega_2 = (4\alpha^2 + 1)(4 - \alpha^2)/5$, it is third order with minimum dispersion. Therefore, by selective control of dissipation and dispersion ($\omega_1 \leqslant \omega \leqslant \omega_2$), the scheme can satisfy different numerical requirements. For the simulation of momentum and temperature, we require some numerical diffusion to suppress short-wave noise and give stable results, so ω is chosen close to ω_2. For scalar advection, we require good conservation of quantities, and ω is set to ω_1.

a. *Time-splitting application*

Huang and Raman (1991) proposed a two-dimensional version of the WKL scheme, which includes a cross-space correction term

$$\frac{\alpha_x\beta_y}{4}(\phi^n_{i+1,j+1} - \phi^n_{i-1,j+1} - \phi^n_{i+1,j-1} + \phi^n_{i-1,j-1})$$

and neglects terms related to α_x^3 and α_y^3 in the original version WKL scheme [Eq. (15)]. Here, α_x and α_y are local Courant numbers in the x and y directions, respectively. However, the numerical stability criterion for this 2D version is reduced to $|\alpha_x, \alpha_y| \leq 0.35$, compared with the maximum Courant number of one in the 1D WKL scheme. The traditional time-splitting method, for example, applying a 1D advection scheme in each direction successively, is simple to implement and more stable since updated values are used along each direction.

Comparisons of the 1D splitting and the 2D HR schemes were performed using a solid body rotational test. An initial cosine cone is assumed to have a base radius of $7\Delta x$ and a height of 20 centered at the point $(13\Delta x, 16\Delta y)$ in a $50\Delta x \times 50\Delta y$ grid interval domain with $\Delta x = \Delta y = 1$ (cf. Fig. 1a). The cone is advected by a rotational flow defined as

$$u(i,j) = -\Omega(y - y_0); \quad v(i,j) = \Omega(x - x_0), \quad (16)$$

where the angular velocity is $\Omega(=0.2\ \mathrm{s}^{-1})$, (x_0, y_0) is the domain center. With the time step $\Delta t = 0.1$ s, the Courant number at the cone center is 0.25 and one full revolution takes 314 time steps. This kind of test should illustrate the shape preservation and dispersion properties in a zero background environment.

Figure 1b shows the result of HR's modified 2D WKL after two full revolutions. At one corner of the domain, the advection becomes unstable after one rotation because the Courant number exceeds 0.35 and the cone diminishes somewhat. By the third rotation, the cone completely disappears. When the two missing terms containing α_x^3 and α_y^3, which are assumed to be negligibly small by HR, are put back into the 2D version WKL scheme, the advection is stabilized and the result is improved as seen in Fig. 1c after four revolutions. This scheme yields two dispersive waves, that is, the positive and negative overshooting rings immediately behind the cone. Figure 2a is the result obtained by the time-splitting 1D WKL scheme. Though numerical dispersion still occurs following the cone, it is less than the 2D version under the same conditions. The time step can be further increased for this 1D splitting until a Courant number of one is reached; this is certainly not the case for the 2D WKL. Therefore, the time-splitting WKL scheme in all three dimensions is chosen for use in this model.

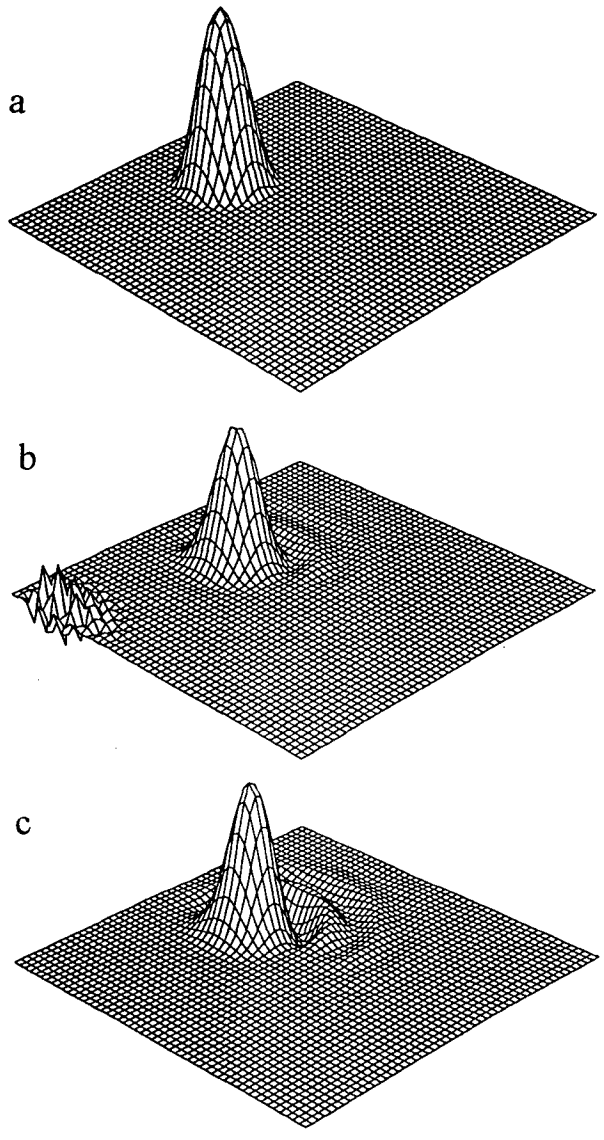

FIG. 1. Results obtained in the solid-body rotational test: (a) initial cosine cone; (b) Huang and Raman's modified fourth-order 2D WKL scheme containing a cross-space correction term after two rotations; (c) after four rotations, adding a_x^3 and a_y^3 terms to Huang and Raman's WKL scheme. (Courant number is 0.25 at the cone center.)

b. Positive definite method

To obtain a positive definite advection scheme, HR and Huang (1994) proposed a variation of the WKL scheme such that positive values are advected with a minimum dissipation of $\omega_1 = 4\alpha^2$; while negative values generated by numerical dispersion are set to zero, and heavy damping with a modified $\omega_2 = 0.8(4\alpha^2 + 1)$ is applied there to reduce adjacent positive value advection. Figure 2b shows the cone advection by the time-splitting 1D WKL scheme using this positive definite method after four revolutions in the rotational flow described above. The negative overshooting is completely deleted, but the positive overshooting is still there following the cone. It is obvious that the diffusion introduced by $\omega = \omega_2$ is not strong enough to damp positive overshooting. The sum of gridpoint values, that is, $\Sigma\Sigma(\phi_{i,j})$ is calculated to represent the total mass

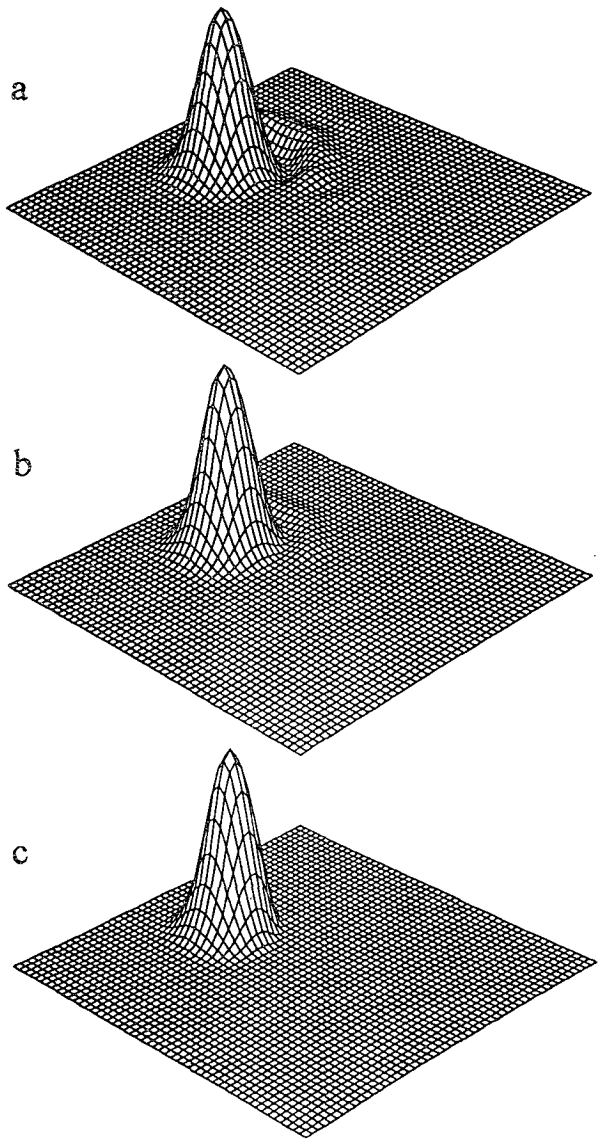

FIG. 2. Same as in Fig. 1 but using the time-splitting 1D WKL scheme after four rotations: (a) with no filter; (b) using Huang and Raman's positive definite method of selective control parameter (ω); (c) using Seibert and Morariu's mass conserving short-wave filter.

of the scalar quantity and we find that the sum after four rotations is 115% of the initial one. Similarly, in Huang's box rotational-flow test (1994) using this algorithm, the ratio of $(\Sigma\Sigma(\phi_{i,j})/\Sigma\Sigma(\phi^0_{i,j})$ is 132% after two revolutions. Sun (1993) criticized this selective control ω method as not being really mass conservative, and pointed out that a constant coefficient 0.8 in HR's modified ω_2 results in truncation error increase as Δt approaches zero. On the other hand, a spacial dependence of ω as introduced in this selective control method can cause errors in advection according to Warming et al. (1973).

In our model, we use the original definitions of ω_1 and ω_2 [cf. Eq. (15)]. For momentum we choose $\omega \approx \omega_2$. For scalars, we choose $\omega = \omega_1$ coupled with a short-wave filter (Seibert and Morariu 1991). With this filter, the short-wave noise occurring on a field with zero background is removed and the net mass obtained from deleting both positive and negative overshoots is redistributed proportionally to the advected quantity to achieve a mass conservative and dispersion-free field. The filter is applied directly after the advection in each direction. Figure 2c shows the result obtained by using Seibert and Morariu's mass conserving filter. After four revolutions, the cone is almost identical to the initial one (Fig. 1a) without any spurious overshooting noise existing on the zero background. The calculation indicates that the sum of gridpoint values of scalar quantity is only 101% of the initial in this test. The time-splitting WKL scheme plus this filter also works effectively in realistic cases, such as a cloud-shape passive scalar being advected over a bell-shaped mountain, as shown in Fig. 3. In this experiment, an initial condition of 10 m s^{-1} upstream wind speed and constant potential temperature is prescribed. Throughout the 14-h integration, the total mass of the cloud remains nearly con-

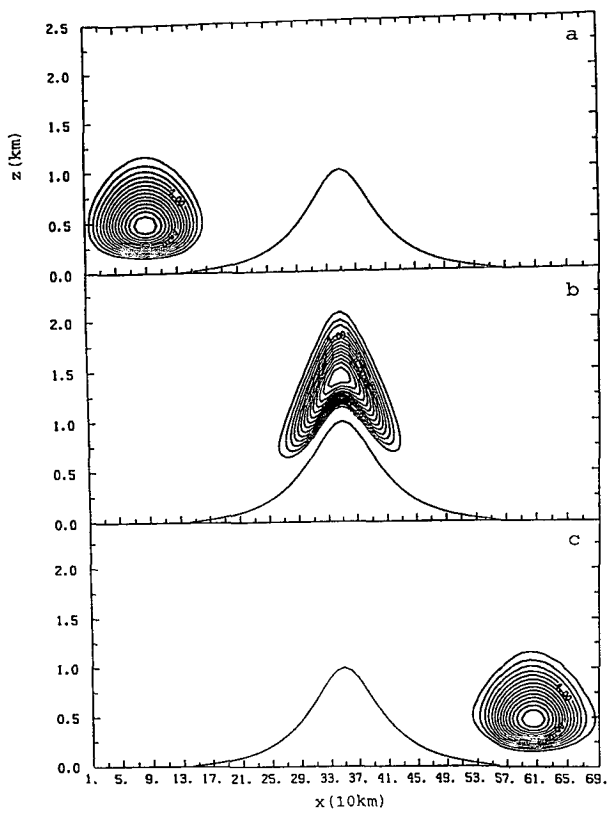

FIG. 3. Contours of passive scalar advected by the fourth-order time-splitting WKL scheme with Seibert and Morariu's filter applied. Initial wind speed is 10 m s^{-1} at upstream boundary and neutral stability: (a) initial cloud; (b) after 4 h; (c) after 14 h.

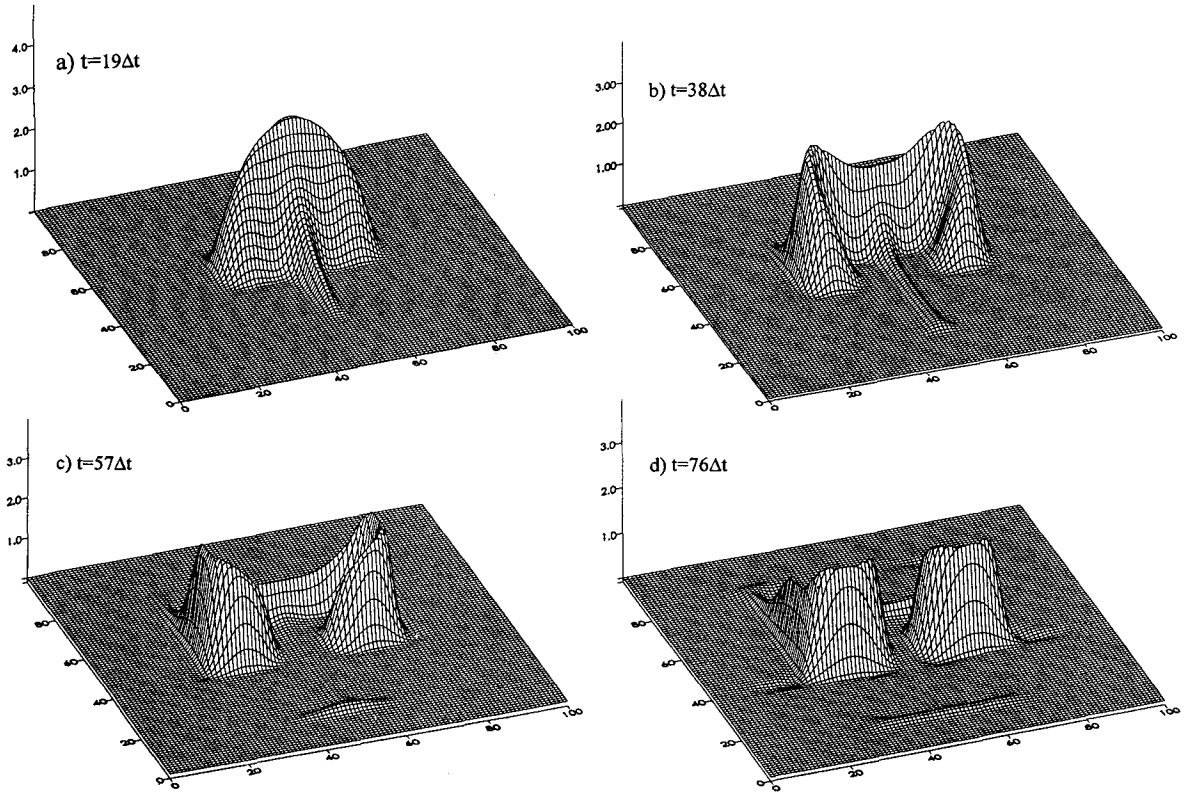

FIG. 4. Results of an initial cone advected by the WKL scheme in the deformational flow test after 19, 38, 57, and 76 iterations.

stant in this pure advection case. After the cloud moves over the mountain, it gradually recovers to its initial shape in this neutrally stratified flow.

c. *Deformational flow test*

To examine the numerical stability of the WKL scheme, we follow Smolarkiewicz (1982) and define the deformational flow by a streamfunction

$$\chi(x, y) = 8 \sin\left(\frac{4\pi x}{L}\right) \cos\left(\frac{4\pi y}{L}\right), \qquad (17)$$

so that the velocity components are

$$u(x, y) = \frac{32\pi}{L} \sin\left(\frac{4\pi x}{L}\right) \sin\left(\frac{4\pi y}{L}\right)$$

$$v(x, y) = \frac{32\pi}{L} \cos\left(\frac{4\pi x}{L}\right) \cos\left(\frac{4\pi y}{L}\right), \qquad (18)$$

where $L = 100\Delta x = 100\Delta y$ ($\Delta x = \Delta y = 1$) in this test. A conical hill of 3.87 high and $15\Delta x$ in radius at the base is located in the center. The time step $\Delta t = 0.7$ s, giving a maximum Courant number of 0.7. The velocity field is constructed with sets of vortices such that the adjacent cells rotate in opposite directions.

Staniforth et al. (1987) presented the analytical solution of this deformational flow advection, with which a numerical calculation can be compared for a short time integration when the space scales of the analytical solution are still resolved by the numerical grid mesh (Bott 1989). Figures 4a–d show the numerical solutions of the third-order-accurate WKL scheme after 19, 38, 57, and 76 iterations. This test reasonably reproduces the main features of corresponding analytical results presented in Fig. 3 of Staniforth et al. (1987). The WKL scheme demonstrates excellent symmetry as shown in Fig. 5, that is, the isolines of scalar concentration at $t = 76\Delta t$, and it holds this behavior throughout the advection process due to the initial scalar distribution and the symmetrical velocity field.

Figure 6 presents the numerical result at $t = 3768\Delta t$ that reveals the initial cone splitting during deformation and disappearing after long time integration. The ratio of the integrated square of gridpoint values $\Sigma\Sigma\phi^2(i, j)$ after 3768 iterations to the initial one is 0.00595. It is clear that the total mass of the scalar keeps decreasing and approaches zero as it should. Therefore, the third-order WKL scheme proves to be very stable in this strongly deformational flow test. The scheme remains stable for $\omega_1 < \omega \leqslant \omega_2$. As mentioned earlier, the third-order WKL is applied to the advection of momentum and temperature fields to damp nonphysical modes,

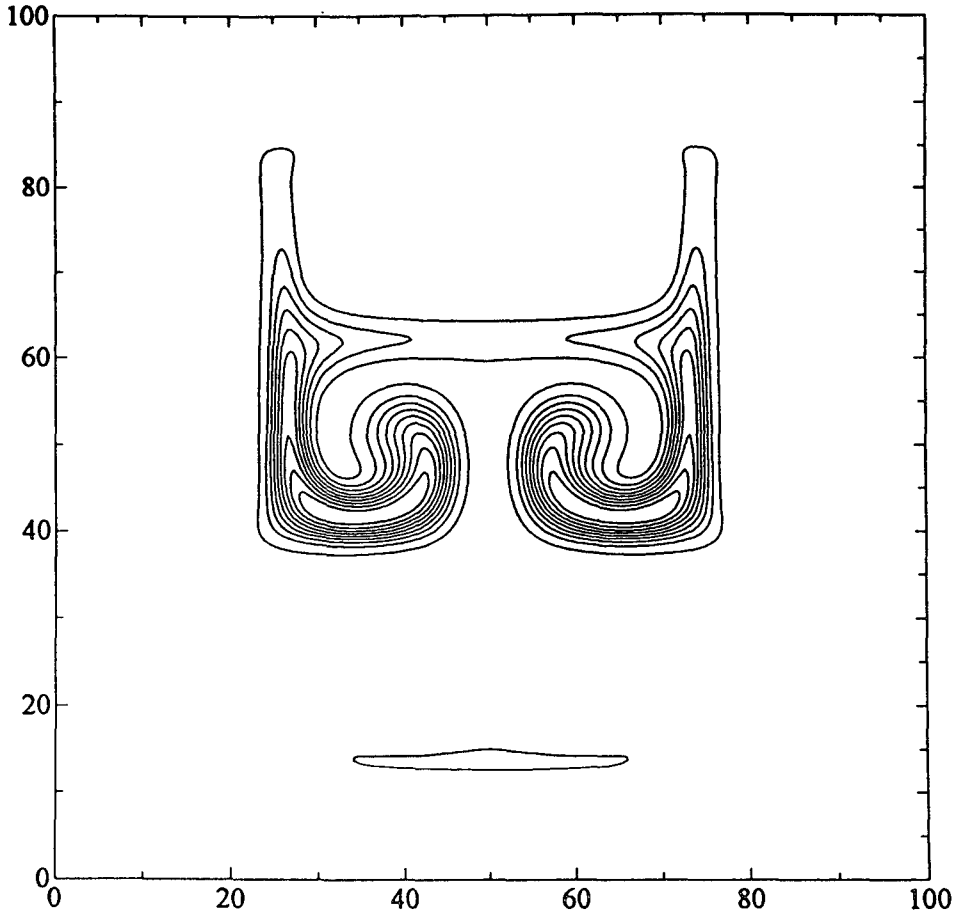

FIG. 5. Isolines of the scalar distribution after 76 iterations shown in Fig. 4d.

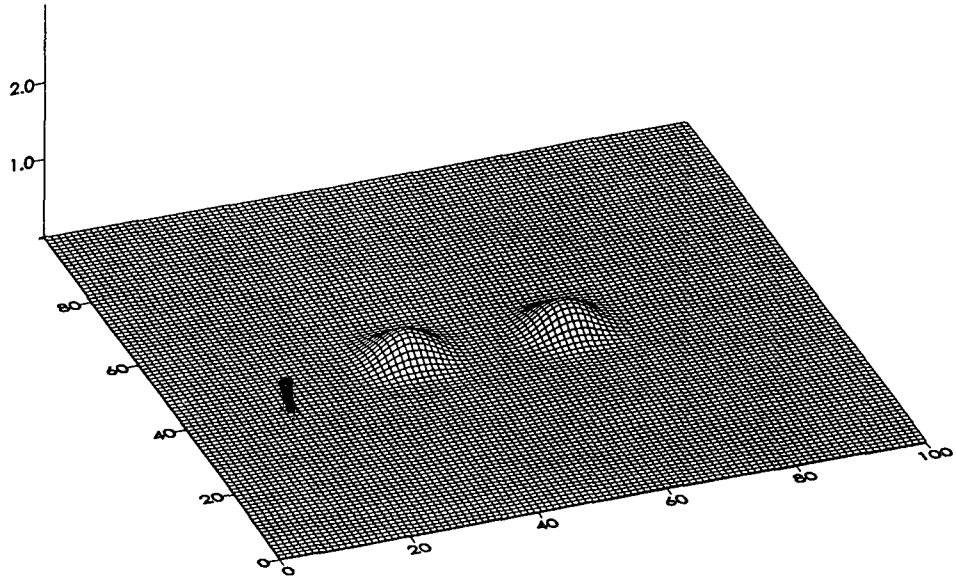

FIG. 6. Same as in Fig. 4 but obtained after 3768 iterations.

while the fourth-order form is applied to scalar quantities to preserve mass. In most atmospheric situations, strong deformational flow fields do not persist for long times, hence, we expect this scheme to be stable for a wide range of flow conditions.

4. Numerical experiments

This model is used to simulate airflows and passive scalar transport over a bell-shaped mountain to examine the model's ability to predict realistic turbulent boundary layer variations and passive scalar dispersion over sloped surfaces. The numerical experiments described below are computed in two-dimensional space by assuming horizontal homogeneity in the north–south direction (y axis). The mountain is arbitrarily located at 38°N (cf. Fig. 7) and the initial model time is 0600 LST 1 April. The initial potential temperature field is prescribed with a vertical gradient of 3.3 K km^{-1} in dry air. The geostrophic wind is set as westerly ($u_g > 0$) and constant in time and in the x direction. The initial winds are obtained by a power-law wind profile in a prescribed nocturnal boundary layer 100 m deep. The wind speed varies from zero at $z^* = 0$ to the geostrophic value for $z^* > 100$. Once computations begin, surface heating/cooling and turbulent transfer quickly change these initial conditions and the model goes through a self-adjustment to reach dynamic equilibrium. Results are presented here for two cases with different initial wind speeds, that is, different geostrophic winds, but using the same initial temperature distribution.

a. Geostrophic wind of 0.5 m s^{-1} without vertical shear

In this case, the simulations are made under the condition of very weak background wind in order to specifically examine thermally induced air flows on both sides of the mountain. During the daytime, the mountain surface is warmer than the air adjacent to the slope and this differential heating produces horizontal pressure gradients toward the mountain and upward motions along the mountain slopes, which increase until evening.

Figure 7 shows the calculated potential temperature θ and zonal component u at 1600 on the second model day. In Fig. 7a, the air at the top of the mountain appears as a soaring thermal plume surrounded by strong horizontal temperature gradients above the mountain slopes. Figure 7b clearly shows that upslope motions develop along both sides of the mountain and strong convergence occurs at the mountain top. Above those updrafts, compensating motions occur as a mass conservation requirement. Far from the mountain, a vertically well-mixed thermal and momentum layer is present over the flat terrain.

During the nighttime, the slope cools much faster than the air around it. The ground-based inversion layer

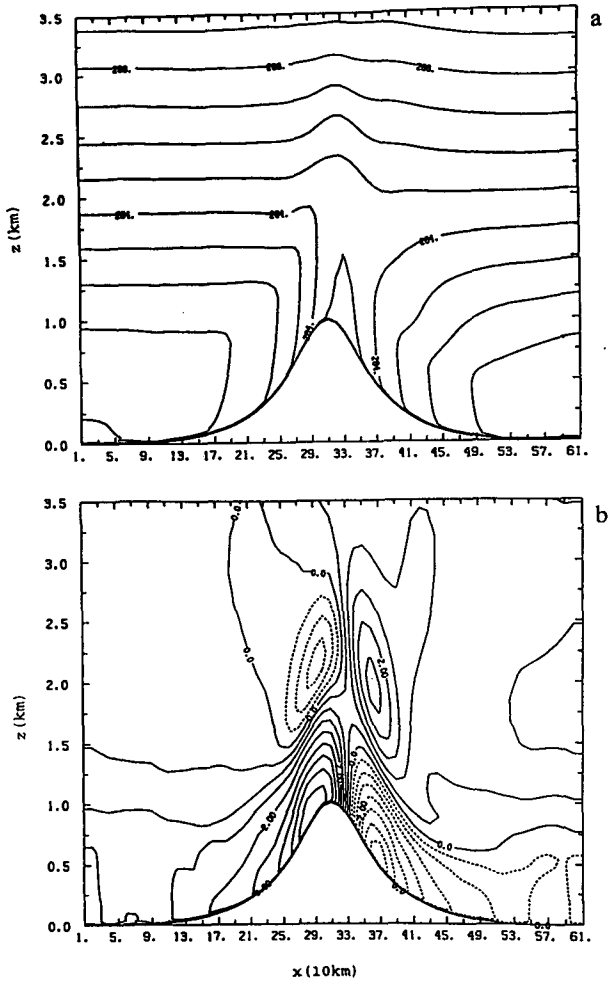

FIG. 7. Results at 1600 LST on the second model day obtained with an initial 0.5 m s^{-1} upstream wind with no vertical wind shear: (a) θ contours, (b) u component. (Solid lines are westerly and the dashed are easterly with a contour interval of 0.5 m s^{-1}.)

produces downslope motions near the surface in response to negative buoyancy. The sinking motions increase as the radiative cooling continues and reach their maximum in the early morning. Figure 8 shows the contours of θ and u at 0600 on the third day. The drainage flows clearly occur on both sides of the mountain, being stronger on the lee side. This asymmetry is due to the background westerly flow. In Fig. 8b, it can also be seen that the return flows occur above the drainage flows. For mass continuity, some air is required to supply the drainage flows. To bring air downward through the stable layer aloft, the drainage flows need to do work against negative buoyancy. It appears to be more efficient to bring air upslope on the lee side through the nearly neutral or slightly stable residual layer above the surface inversion than to draw air down above the mountain top. The return flow on the windward side is automatically enhanced by the background westerly

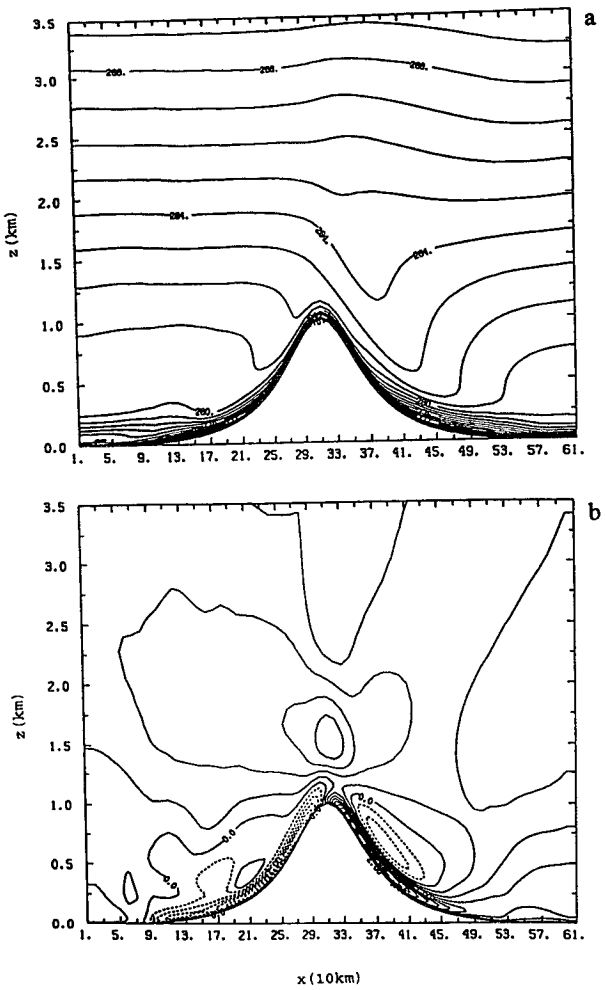

FIG. 8. Same as in Fig. 7 but at 0600 LST on the third model day: (a) θ; (b) u component.

wind. On the other hand, the drainage flows cause adiabatic warming in the temperature field near the surface inversion layer as seen in Fig. 8a, especially on the lee side, as it is enhanced by the background downward motion.

In addition to reproducing the PBL structure and fluxes, the high resolution in the lower part of the domain enables the model to resolve vertical details of the slope flows and reveal detailed thermal and dynamic structures above the mountain slopes.

b. Geostrophic wind increases from surface 0.5 m s^{-1} to 10.5 m s^{-1} at 2 km with 0.005 s^{-1} vertical shear

In this case, a continuous ground-level emission of inert pollutant from an area 50 km wide is set to the west of the mountain. With the imposed certain initial wind conditions, we can examine the behavior of plume diffusion in the turbulent boundary layer and transport over the mountain. Figures 9 and 10 show contours of the plume concentration successively from the first model day to the second.

By the first model day afternoon (Fig. 9a at 1600), the plume has spread upward as the mixed layer grows and is moved uniformly eastward by a vertically constant wind field within the mixed layer. In the evening and early night (Fig. 9b at 2000), the upper part of the plume moves faster than the lower part in the shear flow over the windward side of the mountain. From midnight to early morning (cf. Figs. 9c, 10a, and 10b at 2400, 0400, and 0800 on the second day), the elevated plume continually advances over the mountain with time, while a clean air layer moves downslope in the drainage flow beneath the plume. This clean air layer is maintained during the early morning by the nocturnal inversion layer that prevents mixing of the plume to the surface. In the late morning and afternoon, fumigation

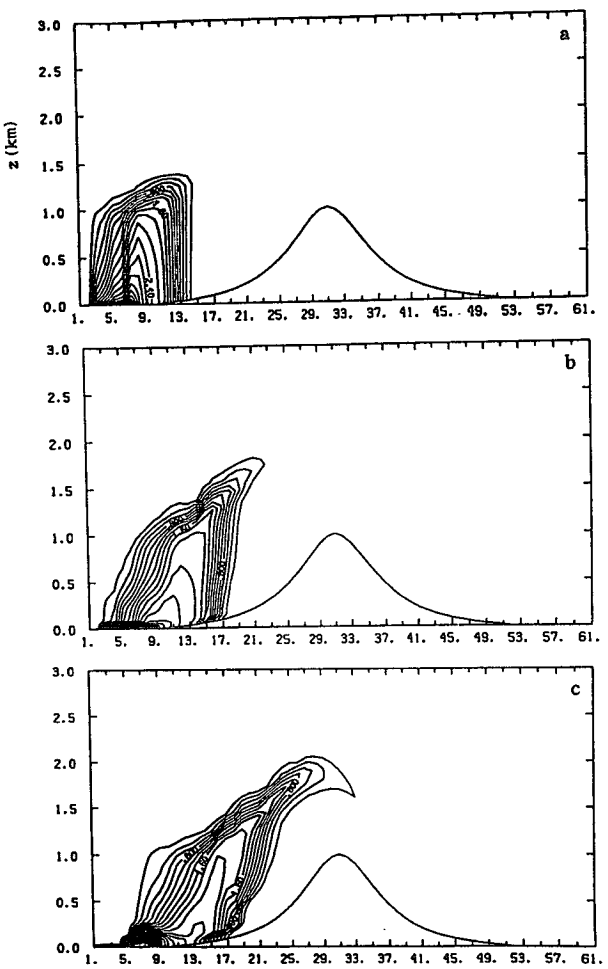

FIG. 9. Calculated concentration contours of the plume obtained with an initial upstream wind of 0.5 m s^{-1} at the surface and increasing upward with 0.005 s^{-1} vertical shear on the first model day: (a) 1600 LST, (b) 2000 LST, (c) 2400 LST. (Contour interval is 0.2.)

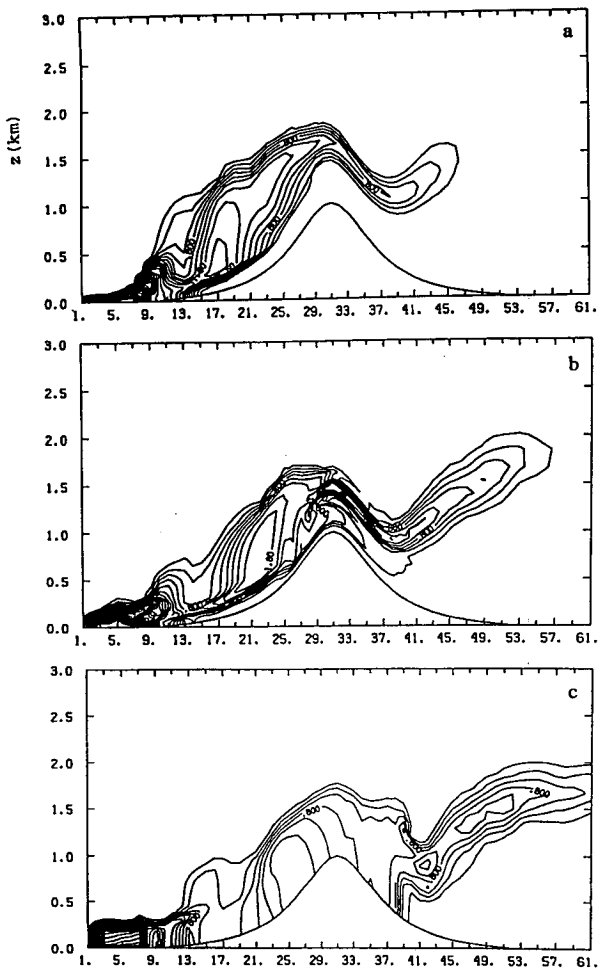

FIG. 10. Same as in Fig. 9 but on the second model day: (a) 0400 LST, (b) 0800 LST, (c) 1200 LST.

occurs and the elevated plume is diffused downward to the surface as the mixed layer grows upward. Consequently, the concentration tends to become constant in the mixed layer over the mountain as seen in Fig. 10c for 1200 of the second day.

Dry hydrostatic mountain waves persist in the free atmosphere above the PBL throughout the diurnal cycles as shown in Fig. 11, that is, the calculated θ field at 0400 on the second day. These waves are generated by the vertical motions over the mountain and extend to the top of model's physical domain. On the lee side, the strong downward flow compresses the depth of the residual or isothermal layer, and the plume is forced to move down the slope, confined by the stably stratified air aloft (cf. Fig. 10). Farther down the slope, the plume jumps up as it is advected forward, when the kinetic energy of airflow is converted to potential energy and the boundary layer expands in depth. Hydrostatic mountain waves force high concentrations locally on the lee side. By making the mountain higher and narrower, such that the slope steepness is doubled, the distributions of temperature, momentum, and pollutant with respect to the mountain are essentially the same as in Figs. 9 and 10.

This sequence of pollutant variation on the upwind side has been observed in a field study in the vicinity of Yosemite National Park on the western side of the Sierra Nevada (Carroll and Baskett 1979). The data are aircraft measurements made on 26 and 27 July and 29 and 30 August in 1973 along a west–east-oriented line from the Central Valley to Yosemite. The airflow over the western slope of the Sierra is often characterized by a well-developed mountain–valley wind system plus extended sea breeze from the San Francisco Bay area. The upslope flow and the extended sea breeze bring the pollutants from the Central Valley to the Si-

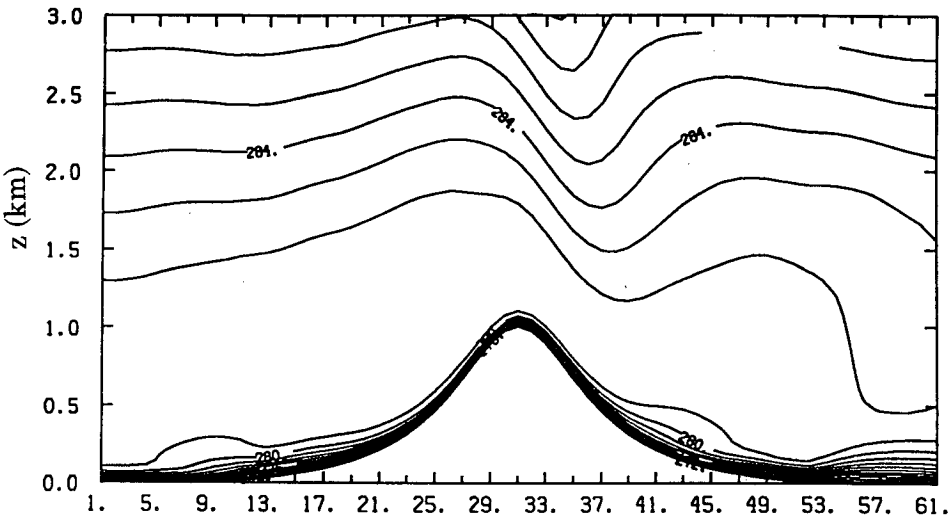

FIG. 11. Same as in Fig. 9 but potential temperature distribution at 0400 LST on the second model day.

erra foothills and transport them up to the mountains at the average wind speed of 3–5 m s^{-1}.

Figure 12 presents the vertical cross section of ozone mixing ratio for 26 July and 29 August of 1973 in three time periods. Both days followed several day periods when the diurnal mountain–valley winds and extended sea-breeze circulations were suppressed by the synoptic-scale pressure field. In the early mornings of both days (i.e., 0600–0900), there existed layers of low pollutant concentration over the western slopes, where the concentrations increase with height within 500 m of the surface. The early morning downslope flow, measured at an average speed of 1.5 m s^{-1}, appears to bring clean air from higher altitudes, creating a thin clean air layer above the surface. Chemical reactions with other species near the surface might also contribute to reducing the ozone concentration in this layer. Later in the morning and afternoon, thermal convection mixes the pollutants and produces nearly constant concentrations near the slope. These observed characteristics are very similar to those modeled in our simulations (cf. Fig. 10).

We do not have sufficient initialization data to simulate these observations directly. However, the model generates vertical and horizontal distributions similar to those observed. While these comparisons are not a true verification of the model, they do indicate the model's ability to resolve details like those found in nature. We conclude that this high-resolution, hydrostatic model performs well in describing boundary layer development and pollutant dispersion in complex terrain.

5. Summary and conclusions

A relatively simple hydrostatic model using Blackadar's local Ri number–dependent turbulence scheme (1979) coupled with a surface energy budget is described. The model uses a height ratio terrain-following coordinate to treat irregular topography. The lower part

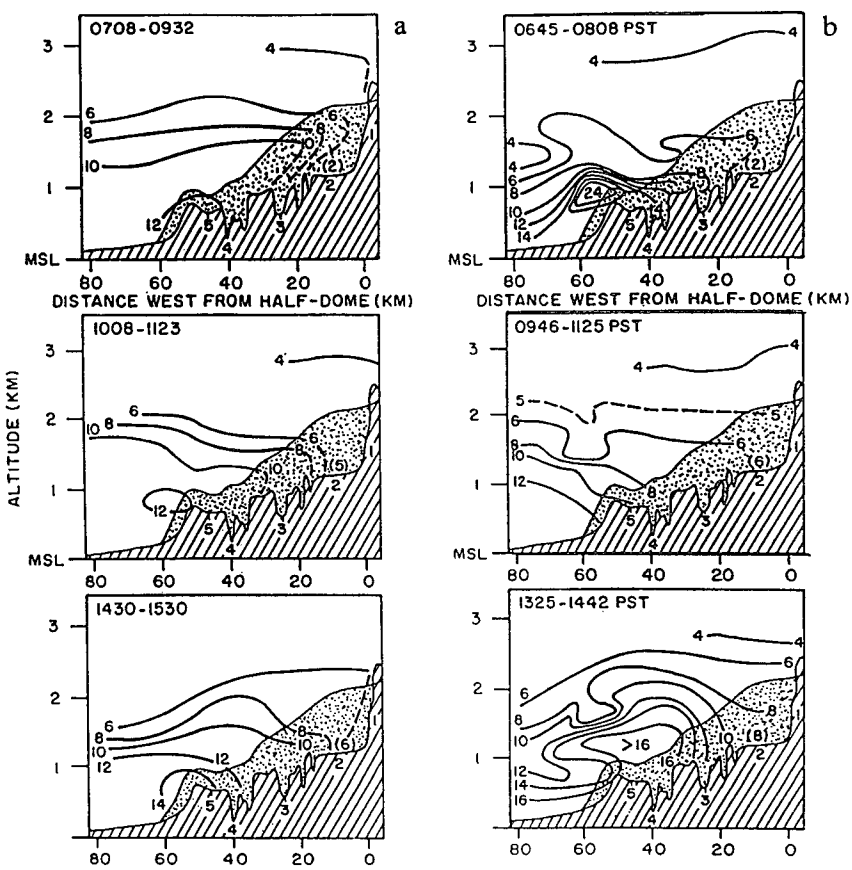

FIG. 12. Observed vertical cross section of ozone mixing ratio contours on (a) 26 July and (b) 29 August 1973. Landmarks identified are 1, Half Dome; 2, Yosemite Valley; 3, El Portal; 4, Briceburg; 5, Mariposa Airport. Lower light line represents topography along the line over the valley, upper light line is smoothed topography at the watershed boundary (after Carroll and Baskett 1979).

of the domain is expanded in a constantly spaced logarithmic coordinate to obtain high resolution near the surface and matched with a fixed Δz outer region to preserve the accuracy of the finite-difference methods used in the model. The analytical integration of hydrostatic pressure of Carroll et al. (1987) is used to minimize the numerical errors related to pressure gradient calculations in the transformed coordinate.

As an important application in this transport model, the third- to fourth-order-accurate, time-splitting 1D WKL advection scheme (Anderson et al. 1984) is compared with a 2D version WKL including a cross-space correction term proposed by HR (1991) in a solid body rotational test. The former is found to be superior with minimal creation of computational modes. The 2D WKL scheme is restricted to a maximum Courant number of 0.35 and limited to two directions requiring another scheme for the third direction. This 2D WKL plus a cross-space term does not really improve the numerical behavior compared with the 1D version. It appears that cross-space corrections can be avoided by using the 1D scheme in a time-splitting technique, which is much more stable and straightforward.

By selective control of the parameter ω, the WKL scheme provides satisfactory solutions to different variable fields having minimum dispersion ($\omega = \omega_2$) or minimum dissipation ($\omega = \omega_1$). When the fourth-order WKL is combined with the mass conserving shortwave noise filter of Seibert and Morariu (1991), the model produces mass conservative and dispersion-free advection for positive definite scalars. This combination works together efficiently each step along each direction. The WKL scheme is also examined in a deformational flow test for its numerical stability and it is found that the scheme holds the stable property from the third order till approaching the fourth order.

The model was initialized with hypothetical, but still realistic, situations to simulate air flows and passive scalar movements over a bell-shaped mountain. The model produces the expected thermal structures of the turbulent boundary layer during the diurnal evolution. The thermally generated mountain–valley wind systems are well developed in the model, revealing detailed local circulations above the mountain slopes, such as drainage and returning flows, which again illustrates the importance of high vertical resolution near the ground. The model predictions show a high degree of similarity to the characteristics observed near Yosemite National Park (Carroll and Baskett 1979), simulating realistic effects of valley winds and mountain waves on air pollutant distributions. The model appears to be well suited for use in moderately complex topography for regional-scale pollutant dispersion studies.

Acknowledgments. This work was supported by the U.S. EPA (R814709) Center for Ecological Health Research at UC Davis. Although the information in this document has been funded wholly or in part by the United States Environmental Protection Agency, it may not necessarily reflect the views of the Agency and no official endorsement should be inferred.

REFERENCES

Anderson, D. A., J. C. Tannehill, and R. H. Pletcher, 1984: *Computational Fluid Mechanics and Heat Transfer.* McGraw-Hill, 599 pp.

Andre, J. C., G. D. Moor, P. Lacarrere, G. Therry, and R. D. Vachat, 1978: Modeling the 24-hour evolution of the mean and turbulent structures of the planetary boundary layer. *J. Atmos. Sci.,* **35,** 1861–1882.

Blackadar, A., 1979: High-resolution models of the planetary boundary layer. *Advances in Environmental Sciences and Engineering,* Vol. 1, J. R. Pfafflin, and E. N. Ziegler, Eds., Gordan and Breach, 50–82.

Bott, A., 1989: A positive definite advection scheme obtained by nonlinear renormalization of the advective fluxes. *Mon. Wea. Rev.,* **117,** 1006–1015.

Businger, J. A., J. C. Wyngaard, I. Lzumi, and E. F. Bradley, 1971: Flux-profile relationships in the atmospheric surface layer. *J. Atmos. Sci.,* **28,** 181–189.

Byun, D. W., 1990: On the analytical solutions of flux-profile relationships for the atmospheric surface layer. *J. Appl. Meteor.,* **29,** 652–657.

Carroll, J. J., 1985: Global transmissivity and diffuse fraction of solar radiation for clear and cloudy skies as measured and as predicted by bulk transmissivity model. *Sol. Energy,* **35,** 105–118.

——, 1993: Sensitivity of PBL model prediction to model design and uncertainties in environmental inputs. *Bound.-Layer Meteor.,* **65,** 137–158.

——, and R. L. Baskett, 1979: Dependence of air quality in a remote location on local and mesoscale transports: A case study. *J. Appl. Meteor.,* **18,** 475–486.

——, L. R-M-Nunez, and S. Tanrikulu, 1987: Accurate pressure gradient calculations in hydrostatic atmospheric models. *Bound.-Layer Meteor.,* **451,** 149–169.

Clarke, R. H., A. J. Dyer, R. R. Brook, D. G. Reid, and A. J. Troup, 1971: The Wangara experiment: Boundary layer data. Tech. Paper 19, 316 pp. [Available from CSIRO, Aspendale, Vic. 3195, Australia.]

Hedley, M., and M. K. Yau, 1988: Radiation boundary conditions in numerical modeling. *Mon. Wea. Rev.,* **116,** 1721–1736.

Huang, C. Y., 1994: Semi-Lagrangian advection schemes and Eulerian WKL algorithms. *Mon. Wea. Rev.,* **122,** 1647–1658.

——, and S. Raman, 1991: A comparative study of numerical advection schemes featuring a one-step modified WKL algorithm. *Mon. Wea. Rev.,* **119,** 2900–2918.

Klemp, J. B., and D. K. Lilly, 1978: Numerical simulation of hydrostatic mountain waves. *J. Atmos. Sci.,* **35,** 78–107.

Liu, M., 1994: Development of a high resolution hydrostatic model suitable for air pollutant dispersion studies in complex terrain. Ph.D. dissertation, University of California, Davis, 104 pp.

Mesinger, F., and Z. I. Janjic, 1985: Problems and numerical methods of the incorporation of mountains in atmospheric models. *Amer. Math. Soc. Appl. Math.,* **22,** 81–120.

Miller, M. J., and A. J. Thorpe, 1981: Radiation conditions for the lateral boundaries of limited-area numerical models. *Quart. J. Roy. Meteor. Soc.,* **107,** 615–628.

Moeng, C.-H., 1984: A large-eddy simulation for the study of planetary boundary layer turbulence. *J. Atmos. Sci.,* **41,** 2052–2062.

O'Brien, J. J., 1970: A note on the vertical structure of the eddy exchange coefficient in the planetary boundary layer. *J. Atmos. Sci.,* **27,** 1213–1215.

Pielke, R. A., 1984: *Mesoscale Meteorological Modeling.* Academic Press, 612 pp.

Purnell, D. K., 1976: Solution of the advective equation by upstream interpolation with a cubic spline. *Mon. Wea. Rev.,* **104,** 42–48.

R.-Mendez-Nuñez, L., and J. J. Carroll, 1993: Comparison of leapfrog, Smolarkiewicz and McCormick schemes applied to nonlinear equations. *Mon. Wea. Rev.,* **121,** 565–578.

Sasamori, T., 1968: Radiative cooling calculation for application to general circulation experiments. *J. Appl. Meteor.,* **7,** 721–729.

——, 1972: A linear harmonic analysis of atmospheric motion with radiative dissipation. *J. Meteor. Soc. Japan,* **50,** 505–517.

Seibert, P., and B. Morariu, 1991: Improvement of upstream, semi-Lagrangian numerical advection schemes. *J. Appl. Meteor.,* **30,** 117–125.

Smolarkiewicz, P. K., 1982: The multi-dimensional Crowley advection scheme. *Mon. Wea. Rev.,* **110,** 1968–1983.

——, 1984: A fully multidimensional positive definite advection transport algorithm with small implicit diffusion. *J. Comput. Phys.,* **54,** 325–363.

Staniforth, A., J. Cote, and J. Pudykiewicz, 1987: Comments on "Smolarkiewicz's deformational flow." *Mon. Wea. Rev.,* **115,** 894–900.

Sun, W. Y., 1993: Comments on "A comparative study of numerical advection schemes featuring a one-step modified WKL algorithm." *Mon. Wea. Rev.,* **121,** 310–311.

Takacs, L. L., 1985: A two-step scheme for the advection equation with minimized dissipation and dispersion errors. *Mon. Wea. Rev.,* **113,** 1050–1065.

Warming, R. F., P. Kutler, and H. Lomax, 1973: Second- and third-order noncentered difference schemes for nonlinear hyperbolic equations. *Amer. Inst. Aeronaut. Astronaut. J.,* **11,** 189–196.

Wippermann, F., 1981: The applicability of several approximations in meso-scale modeling—A nonlinear approach. *Beitr. Phys. Atmos.,* **54,** 298–308.